PHYSICAL REVIEW MATERIALS **4**, 103612 (2020)

Unveiling the atomic-scale origins of high damage tolerance of single-crystal high entropy alloys

Jia Li,[1] Haotian Chen,[1] Quanfeng He,[2] Qihong Fang,[1,*] Bin Liu,[3] Chao Jiang,[1,†]
Yong Liu,[3,‡] Yong Yang,[2,§] and Peter K. Liaw[4]
[1]*State Key Laboratory of Advanced Design and Manufacturing for Vehicle Body, College of Mechanical and Vehicle Engineering, Hunan University, Changsha 410082, People's Republic of China*
[2]*Department of Mechanical Engineering, College of Engineering, City University of Hong Kong, Kowloon Tong, Kowloon, Hong Kong, China*
[3]*State Key Laboratory of Powder Metallurgy, Central South University, Changsha 410083, People's Republic of China*
[4]*Department of Materials Science and Engineering, The University of Tennessee, Knoxville, Tennessee 37996, USA*

(Received 8 April 2020; accepted 6 October 2020; published 26 October 2020)

High entropy alloys (HEAs) exhibit an unusual combination of high fracture strength and ductility. However, atomic mechanisms responsible for crack propagation in HEAs are still not clear, which limits further improving the damage tolerance. Here we investigate effect of crystal orientation on the crack-tip behaviors in single-crystal HEA CrMnFeCoNi using atomic simulations to explore fracture micromechanism. The formation of deformation twinning and activation of multislip systems are observed during the propagation crack with the $(001)\langle 110\rangle$ orientation, consistent with the previous experiments. Under the $(\bar{1}10)\langle 110\rangle$ orientation, the amorphous region takes place throughout the crack growth, and is difficult to occur in traditional metal materials. Dissimilarly, for the $(1\bar{1}\bar{1})\langle 110\rangle$ orientation, the blunting and slip bands occur at the front of the crack tip by switching the slip mode from the planar to wavy slip, observed in recent transmission electron microscopy experiments. The chemical disorder leads to the obvious fluctuation of flow stress, but hardly affects the deformation mechanism at the crack tip. Compared to traditional metals and alloys, the high local stress concentration induced by coupling effect of severe lattice distortion and tension strain leads to the structure transformation from crystallization to amorphization at the crack tip in HEA. While the presented atomic simulations and the associated conclusions are based on CrMnFeCoNi HEA, it is believed that the current deformation mechanism at crack tip could also be applied to other face-centered-cubic HEA.

DOI: 10.1103/PhysRevMaterials.4.103612

I. INTRODUCTION

High-entropy alloys (HEAs) exhibit a number of unique combinations of mechanical properties, such as the high tensile strength, good ductility, and increased corrosion, wear, and fatigue resistance [1–7]. Various processing methods, including mechanical alloying, arc melting, magnetic levitation, and additive manufacturing, have been used to prepare HEAs [8–16]. While their mechanical performance can be initially evaluated by compression, tension, and hardness, their damage tolerance should be obtained to determine their potential for structural applications [1,4,17–20]. Hence, the atomic-scale microstructure-evolution process around the crack tip is a key issue in understanding fracture mechanisms of HEAs. More importantly, the research results related to cracking behavior have generated interest in accelerating their possible use for a wide range of functional and structural applications.

Recently, the damage tolerance of CrMnFeCoNi HEAs has been investigated, which shows the tensile strengths of ∼1 GPa, ductilities of ∼60–70%, and fracture toughness values exceeding 200 $\mathrm{MPa\,m^{1/2}}$ [1,4]. The dislocation slip and twinning to impede crack propagation control the origin of these good properties [1,4]. The dual-phase $\mathrm{Al_{0.5}CrFeNiTi_{0.2}}$ HEAs show that the fracture strength and plastic strain at failure achieved their maximum values of 3.47 GPa and 40%, respectively, owing to the nanoparticle strengthening [21]. The NbMoTaW HEA pillars exhibit the extraordinarily high yield strength of ∼10 GPa and the ductility of compressive plastic strains over 30%, due to stress concentrations at the boundaries to activate dislocation sources in the adjacent grains [22].

The molecular-dynamics (MD) simulations are a powerful tool for investigating the plastic deformation, mechanical properties, and solidification process in HEAs, complementing the current experimental techniques and theories. For instance, using MD simulation, Bahramyan *et al.* studied the plastic deformation mechanism and mechanical properties of transformation-induced plasticity (TRIP) and twinning-induced plasticity (TWIP) HEA and solidified AlCrCoFeCuNi HEA [23–25]. The crystallization kinetics, atomistic clustering-ordering, and dislocation dynamics are investigated in the AlCrCoFeNi HEA [26–29]. The deformation twinning mechanism, phase formation, and nanoscale plasticity are revealed in HEAs [30–32]. Motivated by this, here, MD simulations are employed to characterize the crack propagation of HEA in detail.

The experimental studies mentioned above [1,4,21,22,33,34] reveal that the dislocation slip and twinning

---

[*] fangqh1327@hnu.edu.cn
[†] jiangc@hnu.edu.cn
[‡] yonliu@csu.edu.cn
[§] yonyang@cityu.edu.hk

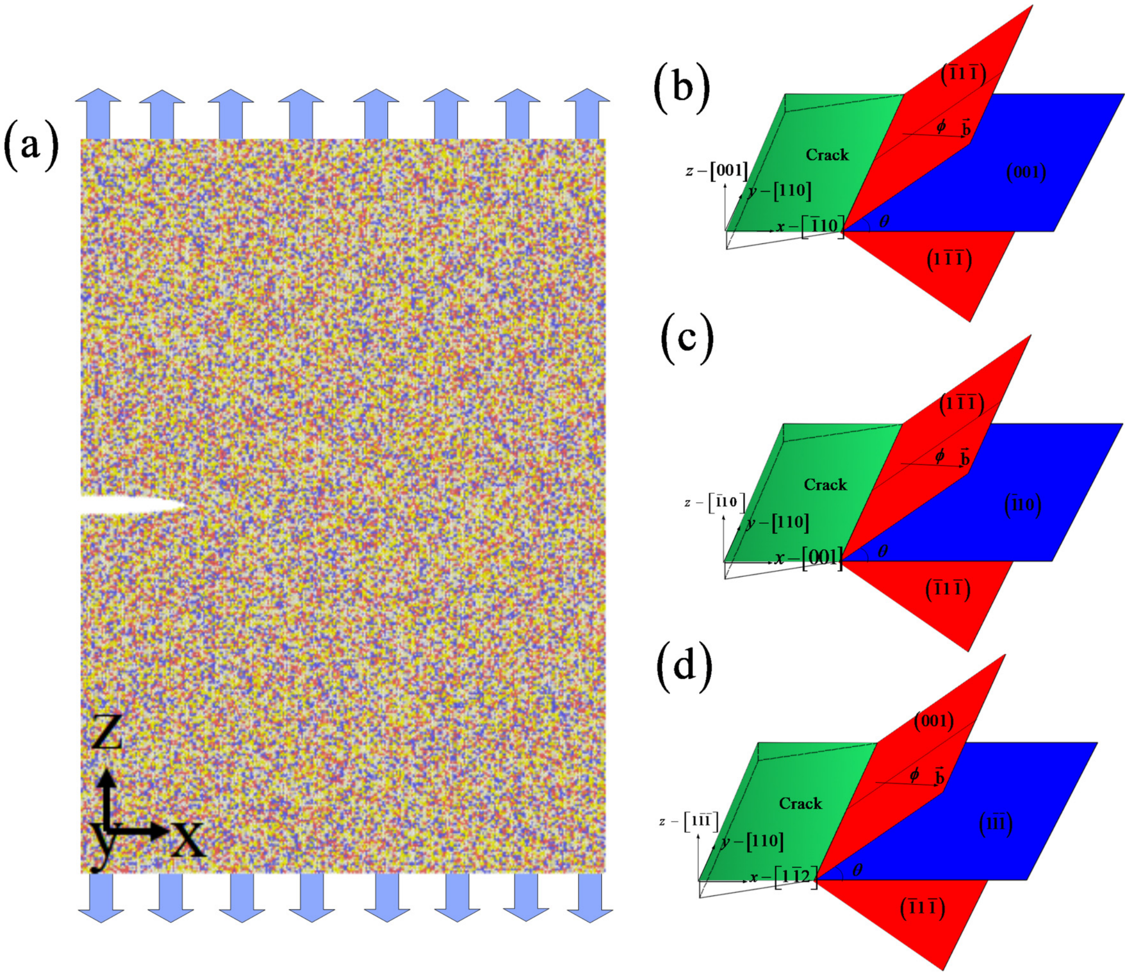

FIG. 1. The single-crystal HEA with the edge crack under a mode-I loading condition (a). ● Co, ● Ni, ● Fe, ● Cr, and ● Mn. Schematic illustration of the type-1 crack with $(001)\langle 110\rangle$ (b), the type-2 crack with $(\bar{1}10)\langle 110\rangle$ (c), and the type-3 crack with $(1\bar{1}\bar{1})\langle 110\rangle$ (d).

formation from the crack tip in HEA. However, these studies are limited to the deformation mechanism at the crack tip, which do not quantitatively establish the relationship between damage tolerance and crack propagation at various crystal orientations. Particularly, the following issues should be well explained: What makes HEAs possess excellent fracture toughness at low temperatures? What is the effect of severe lattice distortion on the fracture mechanisms in HEAs? How does the crack-plane orientation affect crack propagation (see Fig. 1)? Based on the previous experimental observations [1,4,33,34], the present work is committed to addressing the above issues by studying the crack-tip behavior in a single-crystal HEA thin film with a precrack using atomic simulations. Furthermore, atomic simulations can directly provide the atomistic-level understanding of crack-tip events, thereby shedding light on the failure mechanisms of HEAs.

II. METHODS

A. Molecular-dynamics simulations

Here, we build a preexisting edge crack embedded in a rectangular CrMnFeCoNi HEA sample [Fig. 1(a)]. In the present simulations, three types of edge cracks studied include the type 1 with $(001)\langle 110\rangle$, the type 2 with $(\bar{1}10)\langle 110\rangle$, and the type-3 with $(1\bar{1}\bar{1})\langle 110\rangle$. Herein, (001), $(\bar{1}10)$, and $(1\bar{1}\bar{1})$ indicate the directions of the crack planes, and $\langle 110\rangle$ indicates the direction of the crack front. For example, for the type 1 with $(001)\langle 110\rangle$ as shown in Fig. 1(b), the crack surface is on the (001) plane, the crack front is oriented along the y direction of [110], and the potential crack extension is in the x direction of $[\bar{1}10]$. The crack is loaded uniaxially in the z direction of [001]. The size of the HEA sample is $500 \times 25 \times 700$ Å^3 along the x direction, the y direction, and the z direction, respectively. The total number of atoms in the simulation box corresponds to about 760 000. The initial crack length is taken to be 100 Å with a maximum opening of 20 Å. In order to avoid the surface effects on the edge-crack propagation, the periodic boundary conditions are imposed in y and z directions. It is noted that this setting is widely used in previous work of MD simulations related to the edge-crack propagation [35,36]. In addition, the nonperiodic boundary condition is applied in the z direction, which is compared to eliminate the effect of boundary conditions on the deformation behavior at crack tip (see Supplemental Material Fig. S1 [37]). The free-boundary condition is applied in the x direction, in order to prevent the vacancy in the crack center from filling with ghost atom from the neighboring cells. In the HEA sample, the velocities of atoms to meet Newton's second law are adjusted to maintain them at an isothermal state using a time step of 1 fs. Here, the temperature of the system remains the invariant value of 77 K based on the previous experimental condition [1], and the strain rate has a constant value of $1 \times 10^8 \mathrm{s}^{-1}$ for tensile loading of the model. The interaction of the CoCrFeMnNi HEA atoms is simulated using a second-nearest-neighbor modified embedded-atom method interatomic potentials [38], which is as a result of a long-term research effort of Lee's research group. In addition, the necessary unary and binary potential parameters have been determined by Lee and his collaborators [39–46], based on fitting to known fundamental material properties of relevant materials. The open source MD code LAMMPS [47] is used in the atomic simulation, and the open visualization tool (OVITO) [48] is used in the postprocessing of the simulation data.

B. Theory-based model

According to Griffith, the critical stress for dislocation emission can be obtained [49,50]:

$$\sigma_G = K_G/\sqrt{\pi l} \tag{1}$$

Here, in the case of negligible plastic deformation, the theoretical value, K_G, is related to the critical energy release rate, G_c, as shown in

$$K_G = \sqrt{EG_c}, \tag{2}$$

where G_c is the change in the elastic strain energy per unit area of crack advance, and E denotes an appropriate elastic modulus. For a completely brittle fracture of a single crystal, $G_c = 2\gamma_{\mathrm{surf}}$ [49], where the surface energy of the newly created surfaces of the unit area is γ_{surf}.

The criterion for the onset of deformation twinning at a crack tip in face-centered-cubic (fcc) metals, by comparing the energies for nucleating a twinning or slip dislocation, is given by the parameter T as [51,52]

$$T = \lambda\sqrt{\gamma_{us}/\gamma_{ut}}, \tag{3}$$

where λ is a factor that is dependent on both the ratio, γ_{sf}/γ_{us}, and the orientation of the slip system of the twinning dislocations with respect to the crack plane. γ_{sf} is the stacking-fault energy, γ_{us} is the unstable stacking-fault energy, and γ_{ut} is the unstable twinning energy. Here, $T > 1$ stands for the onset of the deformation twin, and $T < 1$ means the onset of the slip dislocation. For the twinning at a crack tip [53], namely $T > 1$, this trend suggests that twinning, rather than slip-dislocation emission, is the preferred deformation mechanism.

The behavior of the brittle to ductile transition for the pure mode-I loading can be determined [53]:

$$\alpha = \frac{k_c}{k_e} = \left[\frac{\gamma_{\mathrm{surf}}}{\gamma_{us}}\frac{(1+\cos\theta)\sin^2\theta\cos^2\phi}{4}\right]^{1/2}, \tag{4}$$

where $k_c = \sqrt{\frac{4\mu\gamma_{\mathrm{surf}}}{1-v}}$ is the critical crack loading for cleavage, and $k_e = [\frac{2\mu\gamma_{us}}{1-v}\frac{8}{(1+\cos\theta)\sin^2\theta\cos^2\phi}]^{1/2}$ is the corresponding loading for emission. θ and ϕ represent the angles between the crack plane and the slip plane, and between the dislocation-line direction and the Burgers vector, $\vec{b}$, as shown in Figs. 1(b)–1(d), respectively. Here, the angle of θ is 54.74° in type 1, 35.26° in type 2, and 70.5° in type 3. The angle of ϕ is 0° or 60°.

III. RESULTS

To clearly understand the effect of the crack-plane orientation on the crack-growth processes, Fig. 2 presents the evolution of dislocation and twinning from the crack tip at the different strains of 3, 4, 5, 7, and 10%. As a result, the partial dislocations nucleate, and then slip at the crack tip with a strain more than 3% for the edge crack of $(001)\langle 110\rangle$ and $(\bar{1}10)\langle 110\rangle$ [Figs. 2(a) and 2(b)]. However, for the edge crack of $(1\bar{1}\bar{1})\langle 110\rangle$, at the strain larger than 5%, the partial dislocations begin to nucleate [Fig. 2(c)]. The full dislocation is broken down into two partial dislocations with the stacking fault, and one partial dislocation moves towards to the crack tip in type 1 with $(001)\langle 110\rangle$ [Fig. 2(a)]. As the applied load increases, the partial twinning dislocations slip, resulting in the increase of the deformation twinning region in front of the crack tip [1,4] [twinning shown in the black-line region of Fig. 2(a5)]. Overall, only the single-slip system in $(\bar{1}10)\langle 110\rangle$ is detected at the crack tip [Figs. 2(b1)–2(b5)], and double or multislip systems in $(001)\langle 110\rangle$ and $(1\bar{1}\bar{1})\langle 110\rangle$ are triggered [Figs. 2(a1)–2(a5), 2(c1)–2(c5)].

Especially, the local lattice distortion-induced stress (see Fig. 3) is one of the important reasons for the occurrence of twinning and amorphization at crack tip (Fig. 2). The hydrostatic stress is defined as $\sigma = (\sigma_x + \sigma_y + \sigma_z)/3$, and represents the average stress of three directions' stresses [54]. A large number of hydrostatic stress peaks appear in HEA (Fig. 3). Meanwhile, the obvious stress concentration is observed in the crack surface [55], due to the existence of edge crack and inhomogeneous distribution of chemical elements [3,7]. Figure 4 shows the distribution of strain before deformation, revealing the local lattice distortion [4]. Recent experiment proves the local strain can characterize the degree of lattice distortion [56,57]. The obvious red highlight areas clearly stand for the serious atomic-scale lattice distortion to exist in HEA matrix, which can greatly affect the deformation mechanism [56,57]. For three cases, the high atomic-scale lattice distortion occurs in HEA, which is different from that of traditional alloys. However, this result cannot be observed in traditional metals and alloys [3,4]. Here, the difference of atomic size in HEAs can induce the high friction stress to hinder dislocation motion [3–5], resulting in the twinning and crystallization-to-amorphous transition at a crack tip (see the detailed explanation in Figs. 6 and 7).

In Fig. 5(a), the tensile stress-strain curves of the HEA with the edge crack are plotted with different crack-plane orientations, showing the crack-plane orientation effect on the mechanical properties. High strength and high strain hardening are found in HEA, compared to traditional alloys and pure metals [1,3]. Especially, HEA with the crack of $(\bar{1}10)\langle 110\rangle$ shows the obvious advantage on mechanical property owing to the amorphous formation at crack tip to enhance damage tolerance by increasing the resistance of crack expansion (Figs. 3 and 5). The slope of the stress-strain curve presents Young's modulus, which also depends on the crack-plane orientation. The HEA with the crack of $(\bar{1}10)\langle 110\rangle$ exhibits a higher Young's modulus than the other type cracks, while Young's modulus in HEAs with the crack of $(001)\langle 110\rangle$ is larger than that in HEAs with the crack of $(1\bar{1}\bar{1})\langle 110\rangle$. As well known, the damage tolerance of materials depends on Young's modulus

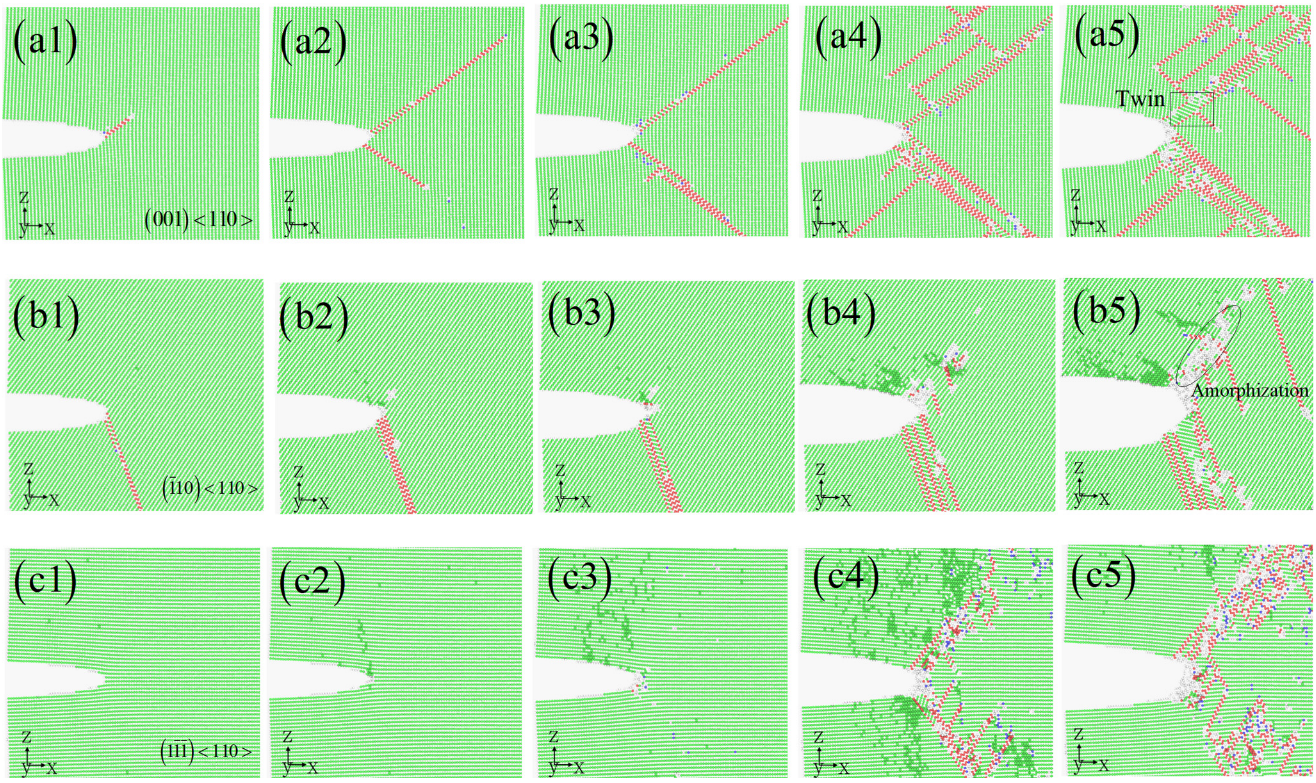

FIG. 2. Crack-propagation processes at the temperature of 77 K, and crack plane: $(001)\langle 110\rangle$ (a1)–(a5), $(\bar{1}10)\langle 110\rangle$ (b1)–(b5), and $(1\bar{1}\bar{1})\langle 110\rangle$ (c1)–(c5). Various strains are 3% (a1)–(c1), 4% (a2)–(c2), 5% (a3)–(c3), 7% (a4)–(c4), and 10% (a5)–(c5). Here, atoms are colored based on the common-neighbor analysis (CNA): ⚪ unknown, 🔴 hexagonal-close-packed (hcp), 🔵 body-centered-cubic (bcc), and 🟢 face-centered-cubic (fcc). The black-line region represents the twinning at the crack tip in (a5), and the black elliptical line region represents the amorphization at the crack tip in (b5).

and strength [1,3,4,58]. Hence, the crack-plane orientations could control resistance of crack propagation within the material, which can largely affect the damage tolerance of HEA.

For the plastic stage, the flow stress at $(1\bar{1}\bar{1})\langle 110\rangle$ is always higher than that at $(001)\langle 110\rangle$. It is evident that the greater stiffness does not necessarily lead to the higher strength, different from traditional viewpoints about the stiffness positive correlation with the strength. The previous work also shows that the simple crystalline solids confer surprisingly the high strength to materials with extremely low elastic constants [59]. These results give viewpoints for the HEA selection and design, replacing the conventional rule that a large Young's modulus is regarded as a reliable predictor about the hardness and strength of materials. In addition, the ductile to brittle transformation in crack plane $(\bar{1}10)\langle 110\rangle$ leads to the lack of strain hardening [58], due to the amorphization.

Switching the slip mode from the single planar slip to the double planar slip reduces the flow stress [Figs. 2 and 5(a)]. As presented in Fig. 5(b), the $(1\bar{1}\bar{1})\langle 110\rangle$ crack surface has the lowest surface energy, meaning the low crack-nucleation resistance is owing to the low critical energy release rate. Here, by Eq. (1) and Figs. 5(a) and 5(b), the critical stress

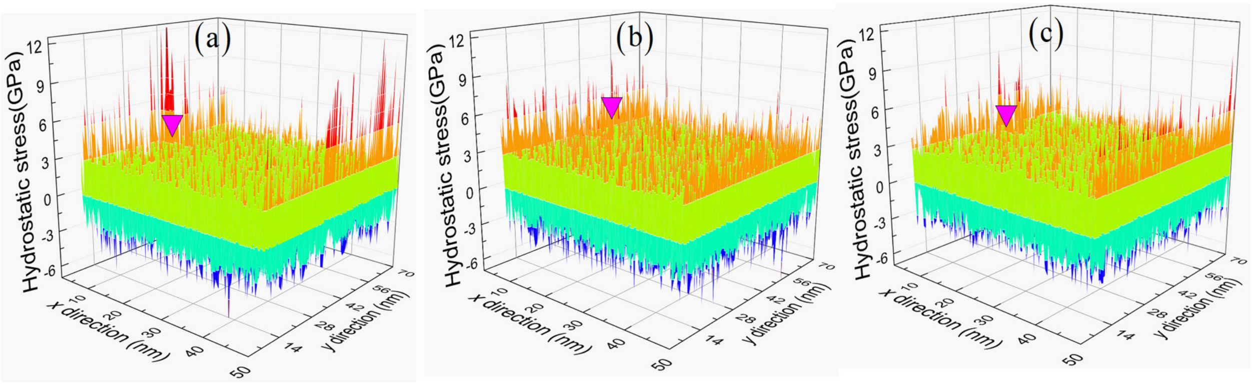

FIG. 3. Distribution of hydrostatic stress at different crack-plane orientations: $(001)\langle 110\rangle$ (a), $(\bar{1}10)\langle 110\rangle$ (b), and $(1\bar{1}\bar{1})\langle 110\rangle$ (c) in HEA. The pink triangle region indicates the crack position.

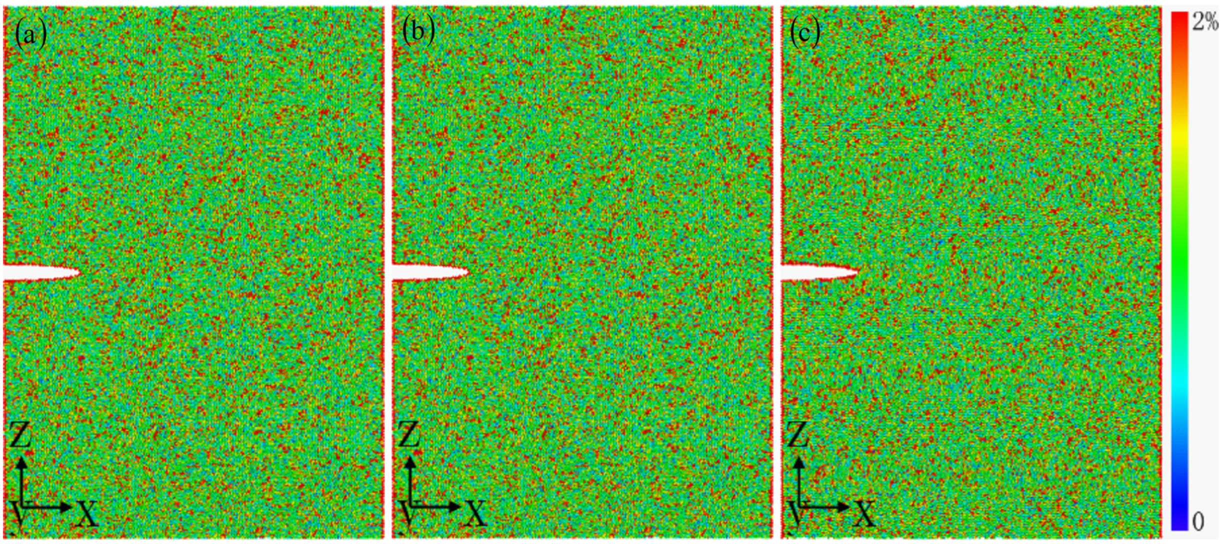

FIG. 4. Distribution of strain at different crack-plane orientations: $(001)\langle 110\rangle$ (a), $(\bar{1}10)\langle 110\rangle$ (b), and $(1\bar{1}\bar{1})\langle 110\rangle$ (c) in HEA. The red atom represents large strain, and the blue atom means low strain.

for the dislocation emission is 3.34 GPa in $(001)\langle 110\rangle$, 3.92 GPa in $(\bar{1}10)\langle 110\rangle$, and 2.49 GPa in $(1\bar{1}\bar{1})\langle 110\rangle$, revealing the high damage tolerance in crack plane $(\bar{1}10)\langle 110\rangle$. The local stress field at the crack tip depends on the lattice-distortion degree, which is produced by the random distribution of different components with various atomic sizes. Compared to the pure metals, the critical stress should be located in a range of value, which is instead of a constant value. Figure 5(c) shows the radial distribution function (RDF) of HEA during loading in a selected crystal/amorphization region. The disappearing RDF peak and broadened RDF further confirm the amorphous characteristic.

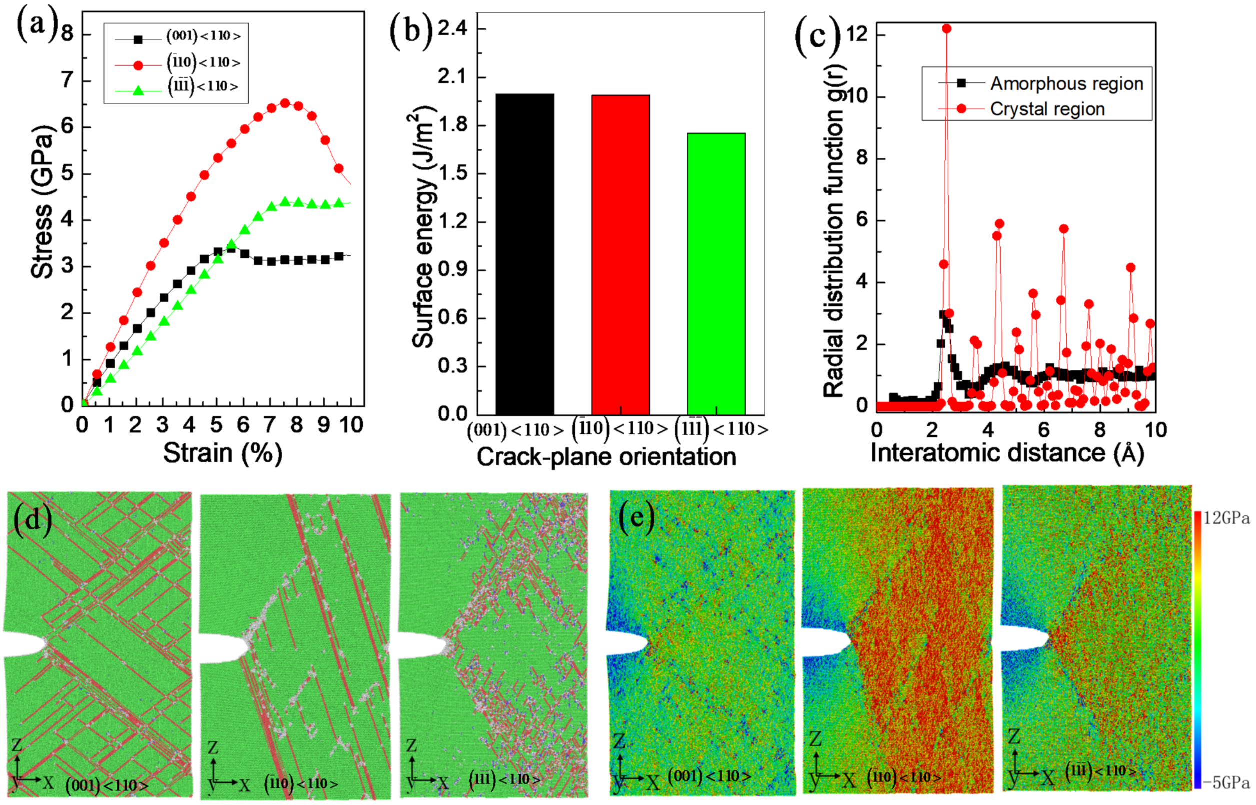

FIG. 5. The stress vs strain at the temperature of 77 K and the different crack-plane orientations: $(001)\langle 110\rangle$, $(\bar{1}10)\langle 110\rangle$, and $(1\bar{1}\bar{1})\langle 110\rangle$ in the HEA (a). Surface energy vs crack-plane orientations (b). Radial distribution function of crystal and amorphous region (c). Microstructure evolution at the strain of 10% and the crack tip (d). The corresponding stress-field distribution along the z direction (e), where the red atom represents the high tension stress, and blue atom represents the low stress.

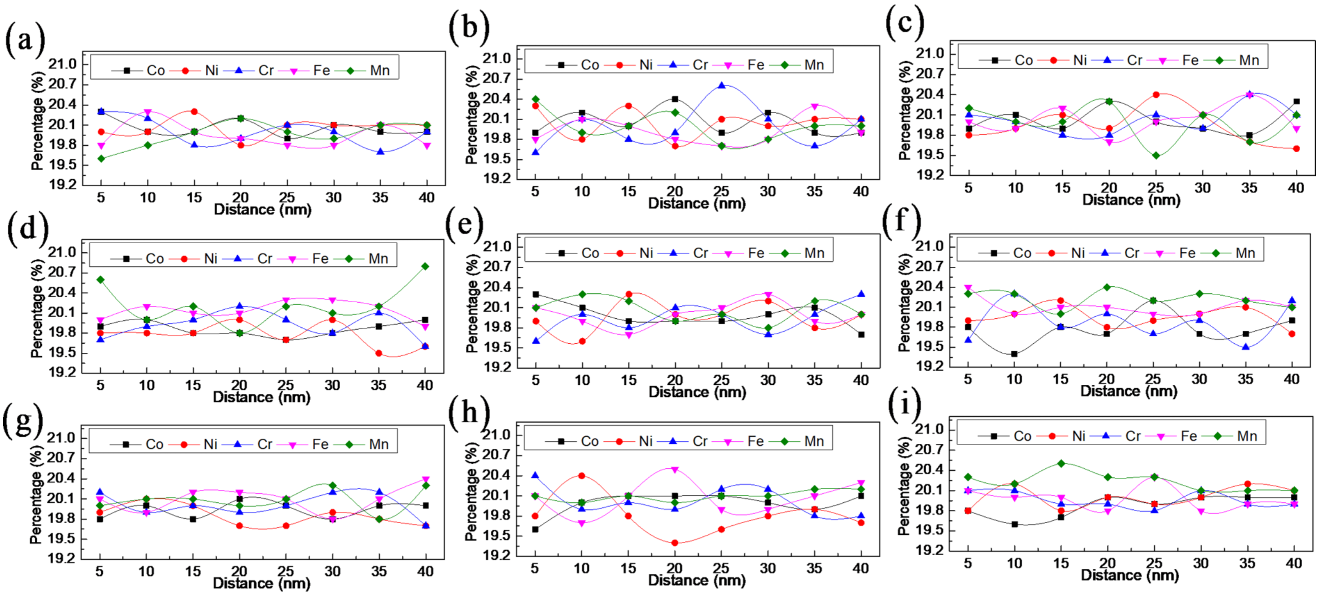

FIG. 6. Element distribution of Co, Ni, Cr, Fe, and Mn along the x direction at the different samples. The different crack-plane orientations are $(001)\langle 110\rangle$ (a), (d), (g), $(\bar{1}10)\langle 110\rangle$ (b), (e), (h), and $(1\bar{1}\bar{1})\langle 110\rangle$ (c), (f), (i).

When the loading stress exceeds the critical stress related to crack propagation, the edge crack extends rapidly in the brittle amorphous region compared to the ductile crystal region [Figs. 2 and 5(d)]. The dominant cracking mechanism changes from the completely brittle to ductile behavior with the dislocation nucleation [Figs. 2 and 5(d)], which complies with the brittle to ductile transition from Eq. (4). The emergence of very small geometric irregularities formed along the crack tip is the prerequisite for the transition from the brittle to ductile appearance (Figs. 2 and 5), in good agreement with the previous results [1,4]. In other words, the severe lattice distortion in HEAs is built into the structure at the atomic level (see Figs. 3 and 4), leading to its good damage-tolerance properties [1,4]. Figure 5(e) presents the obvious differences in the microstructures at the crack tip, to produce the complex stress field [Fig. 5(e)]. The higher stress occurs at the crack with $(\bar{1}10)\langle 110\rangle$ relative to those of $(001)\langle 110\rangle$ and $(1\bar{1}\bar{1})\langle 110\rangle$ in Fig. 5(e), agreeing with the result of Fig. 5(a) about the larger flow stress with the plastic deformation. Hence, the underlying reasons of the deformation twin and slip-band formation have been explained in term of the stress, and it can be attributed to the asymmetry of the stress distribution induced by the severe lattice distortion (see Fig. 3). The hydrostatic stress shows the random peaks in slip plane, which strongly affects the dislocation motion. The strain distribution also proves the severe atomic-level lattice distortion generated in HEAs (see Fig. 4).

The effect of chemical disordering (atom arrangement) on the mechanical properties and crack-tip behavior would be studied. Here, the element distribution of samples with different atom arrangements are presented in Fig. 6 and Figs. S2 and S3 [37]. Three samples show the difference of concentration distribution (see Fig. 6), which results in various degrees of local lattice distortion. Recent experiments have also demonstrated this trend [7,60–62]. The relationship of average stress and strain from three HEA samples is presented in Fig. 7. As a result, the chemical disorder leads to the obvious fluctuation of flow stress, where the maximum error bar is ±0.4 GPa in $(001)\langle 110\rangle$, 0.9 GPa in $(\bar{1}10)\langle 110\rangle$ orientation, and 0.3 GPa in $(1\bar{1}\bar{1})\langle 110\rangle$. Here, the microstructural evolution reveals the deformation mechanism is the same at the crack tip (Fig. 8). Thus, the deformation behavior is independent of the chemical disorder but it is related to the crack-plane orientations. Hence, the randomness of HEA strongly affects the flow stress, but it can hardly change the deformation mechanism at the crack tip.

IV. DISCUSSION

To deeply understand the origin of the dislocation nucleation and deformation twinning at the crack tip, the stacking fault energy of random solid-solution FeCoCrNiMn alloys is calculated in Fig. 9(a), for proving the possibility of occurrence. Both the intrinsic stacking faults (ISF) and extrinsic stacking faults (ESF) are illustrated in Figs. 9(b) and 9(c), where the bulk contains about 1 100 000 atoms by sequentially stacking close-packed (111) atomic planes. An ISF is created by shifting the upper layers along the [112] direction with the Burgers vector of the Shockley partial. Further shifting of the fault leads to the ESF and twinning, as shown in Figs. 9(b) and 9(c). The values of γ_{isf}, γ_{esf}, and γ_{twin} are obtained from the proportion between the energy difference in the original and stacking-faulted structures, and the corresponding area. The calculated values of γ_{isf}, γ_{esf}, and γ_{twin} γ_{twin} are $-47.3\,\mathrm{mJ/m^2}$, $-46.8\,\mathrm{mJ/m^2}$, and $-46.4\,\mathrm{mJ/m^2}$, which agree well with the previous reports [3,63–65]. These three values are very close, indicating the same possibility for the occurrence of dislocation and twinning based on Eq. (3) [64]. In other word, from the point of view of energy, the dislocation and twinning could simultaneously take place at a crack tip.

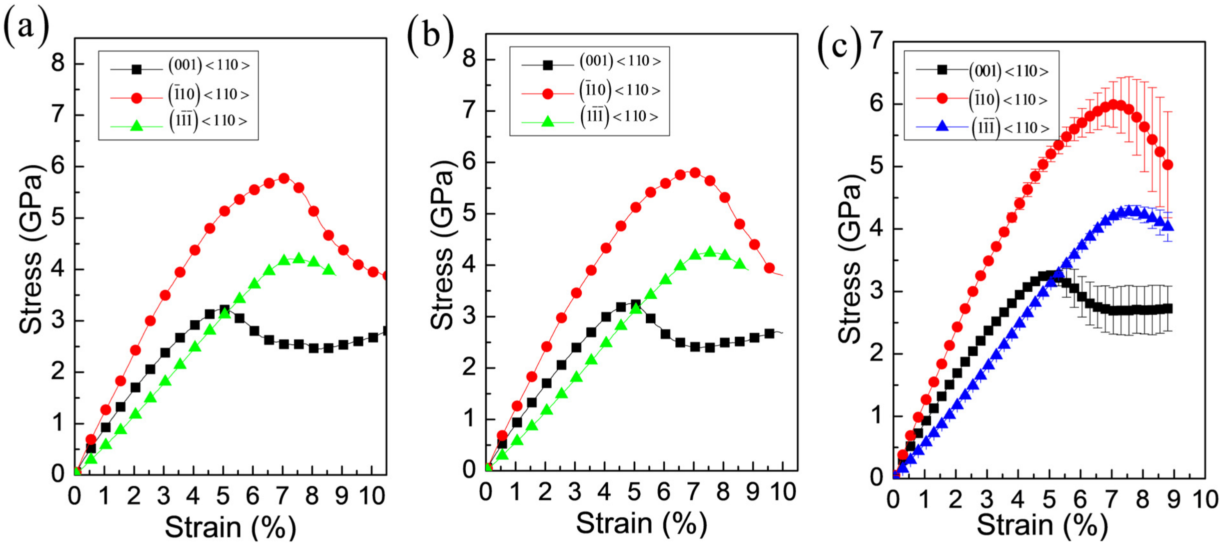

FIG. 7. The stress vs strain at other HEA sample (a), (b). The average stress vs strain from three HEA samples (a), (b).

To reveal the amorphization formation mechanism, the processes of crystal to amorphous phase transformation are divided into two stages based on the microstructural evolution (Fig. 10). When the strain energy produced by defects (point defects, dislocations, and twins) and severe lattice distortion at a crack tip exceeds the maximum elastic energy inside the crystal [Figs. 10(a) and 10(b)], amorphization nucleation occurs due to elastic instability based on Born criteria at high deformation rate [66,67]. With increasing strain, the dislocations continuously generate and interact with small amorphization phase, and then lattice continues to collapse, resulting in the propagation of the amorphization region [Figs. 10(a) and 10(b)] [66,67]. The similar phenomena have been confirmed in NiTi alloys and FeCoCrNi HEA [66,67]. Figure 10(c) shows that τ_1 and τ_2 are shear stresses in the slip-deformation band. The stress, τ_3, causes the crystal to slip along the other slip direction and induces dislocations along this direction when the dislocation cannot slip along the direction of the shear stress, τ_1. However, the shear stress, τ_3, is not located on the slip plane along the slip direction and deviates from a certain angle of the slip system. Thus, these dislocations would be difficult to slip. Under the increasing stress, the lattices around dislocations are further distorted or twisted, and the lattices along the stress direction may also displace each other, resulting in disordered amorphous clusters (Fig. 10). Recently, the deformation behavior of nonequiatomic CrMnFeCoNi HEA at low temperature and tension strain of 28% shows the high density of dislocations stored in shear bands due to the presence of severe distortion [Fig. 11(a)] [68]. Especially, some of shear bands transform into amorphous bands, as demonstrated in Fig. 11(b). *In situ* fracture studies show the crystal to amorphous transformation in NiTi intermetallic compound when the stress at a crack tip is higher than the critical stress for the amorphous nucleation [66]. This reason could explain why amorphous transition occurs in only type-2 crack model with high flow stress compared with other cracks. Finally, the expansion and connection of amorphous clusters form amorphous bands with a width of 1–2 nm in front of the crack tip (see Figs. 2, 5, and 10). Recently, the nucleation of amorphous phases at intersections of SFs/twins has been demonstrated by transmission electron microscopy (TEM) observations in FeCoCrNi HEA during high pressure torsion [69]. More importantly, this trend results in the complex microstructural-evolution model at the crack tip [Figs. 2 and 5(b)], and thus offers a rational design of advanced HEAs by adjusting the elemental concentration.

To understand the mechanism for the crystal-amorphous transition, we consider the following thermodynamics which

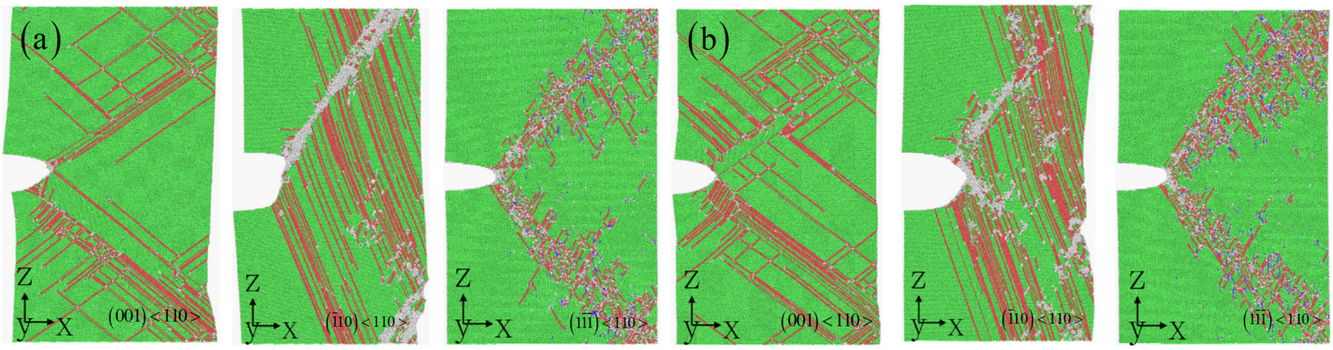

FIG. 8. Microstructure evolution of the crack tip at other HEA sample (a), (b).

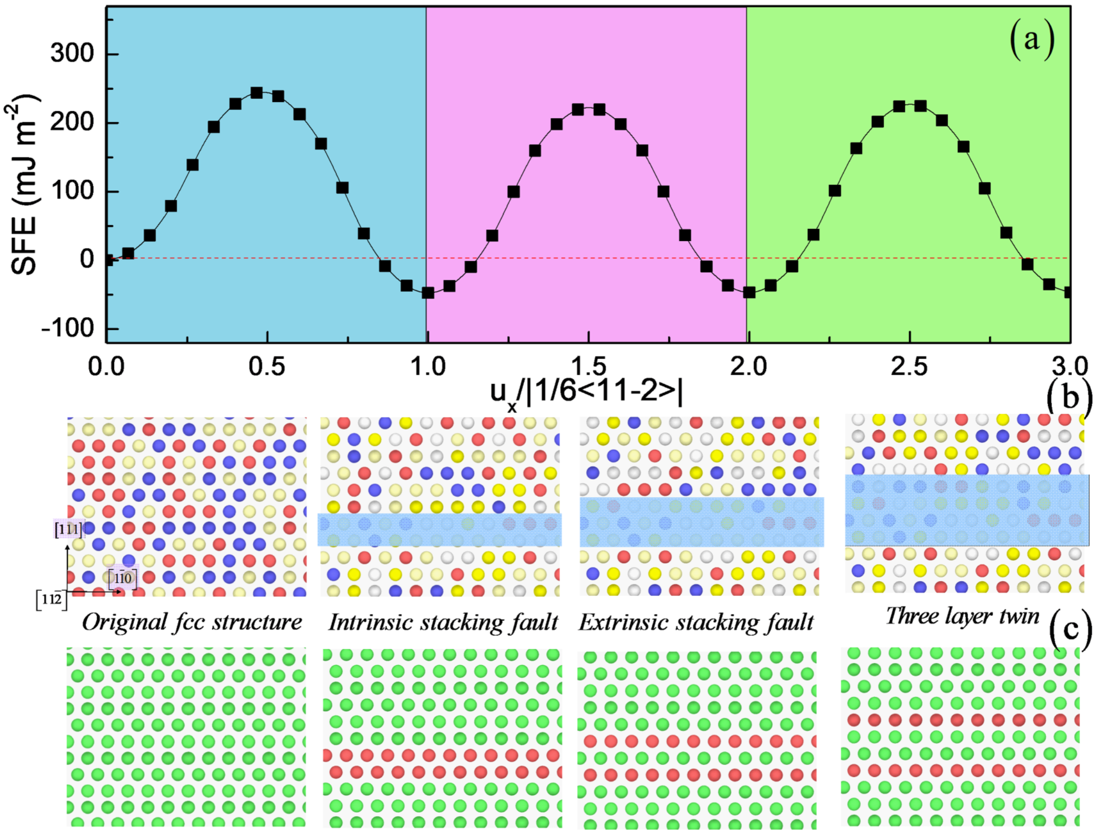

Original fcc structure *Intrinsic stacking fault* *Extrinsic stacking fault* *Three layer twin*

FIG. 9. The interplanar potentials for the HEA and associated atomic configurations. The figure contains the curve in different color regions: (a) the line in the blue region presents the slip along the leading partial direction; the line in the pink region corresponds to the faulted potential for a crystal containing an intrinsic stacking fault; the line in the light-green region shows three-layer twins. u_x is the total slip, including that of the leading partial. The atomic configurations associated with the labeled extrema on the curves are displayed below them (b), (c). The coordinate systems are the x axis along $[1\bar{1}0]$, the y axis along $[11\bar{2}]$, and the z axis along [111].

entails the accumulation of dislocations to a level that the corresponding free energy of a crystal becomes greater than that of a glass. As the dislocation density increases during the deformation process, the dislocations would interact with each other and hinder their further movement. When the dislocation density reaches a critical value, the collective interaction of dislocations would destabilize the crystalline lattice, resulting in a transformation to a disordered state to release the stored strain energy. According to the classical nucleation theory [70], to form a sphere amorphous nucleus with radius r from the crystalline matrix, the total Gibbs free-energy changes ΔG can be expressed as

$$\Delta G = \tfrac{4}{3}\pi r^3(\Delta G_V + \Delta G_{\mathrm{CA}} - E_{\mathrm{dis}} - E_{\mathrm{ela}}) + 4\pi r^2\gamma_{\mathrm{CA}}, \quad (5)$$

where ΔG_V is the volumetric expansion induced free-energy density change, ΔG_{CA} is the free-energy density difference between the crystalline and amorphous phases, E_{dis} is the strain-energy density stored in the accumulated dislocations, E_{ela} is the elastic part of the strain energy, and γ_{CA} is the interfacial energy between crystalline and amorphous phases. The crystalline to amorphous phase transition is only energetically favorable when $\Delta G < 0$ for a large strain energy storage. If we take the first derivation of ΔG with respect to amorphous phase nucleation size r equal to zero, i.e., $\partial\Delta G/\partial r = 0$, the critical radius r_{crit} for stable nucleus can be obtained as

$$r_{\mathrm{crit}} = \frac{2\gamma_{\mathrm{CA}}}{-(\Delta G_V + \Delta G_{\mathrm{CA}} - E_{\mathrm{dis}} - E_{\mathrm{ela}})}. \quad (6)$$

The critical nucleus radius defines a minimal size an amorphous nucleus can survive. Any nucleus with size below r_{crit} would be dissolved into the crystalline matrix. Only these nuclei with size larger than r_{crit} have the possibility to survive and continuously grow. From Eq. (6), the critical radius r_{crit} is a function of stored strain energy. As the increase of strain energy storage, the critical radius r_{crit} would decrease continuously, which makes it easier for the crystalline to amorphous phase transition.

According to our simulation result, the interfacial energy between crystalline and amorphous phases γ_{CA} is about $483.87\,\mathrm{mJ/m^2}$ for CoCrFeMnNi HEA. According to Eshelby's theory [71], the volumetric dilatation-induced misfit energy ΔG_V can be expressed as $\Delta G_V = K(1-2v)(\Delta V/V)^2/[3(1-v)]$, where K is the bulk modulus which is about 140 GPa [72], v is Poisson's ratio which is about 0.26 [72], $\Delta V/V$ is volumetric dilatation strain which is about 2.3% based on our simulation results. Besides, the Gibbs free-energy difference of crystalline and amorphous phases ΔG_{CA} is about 4.35 kJ/mol according to our calculations. The strain energy stored in the accumulated dislocations E_{dis} can be expressed as [73]

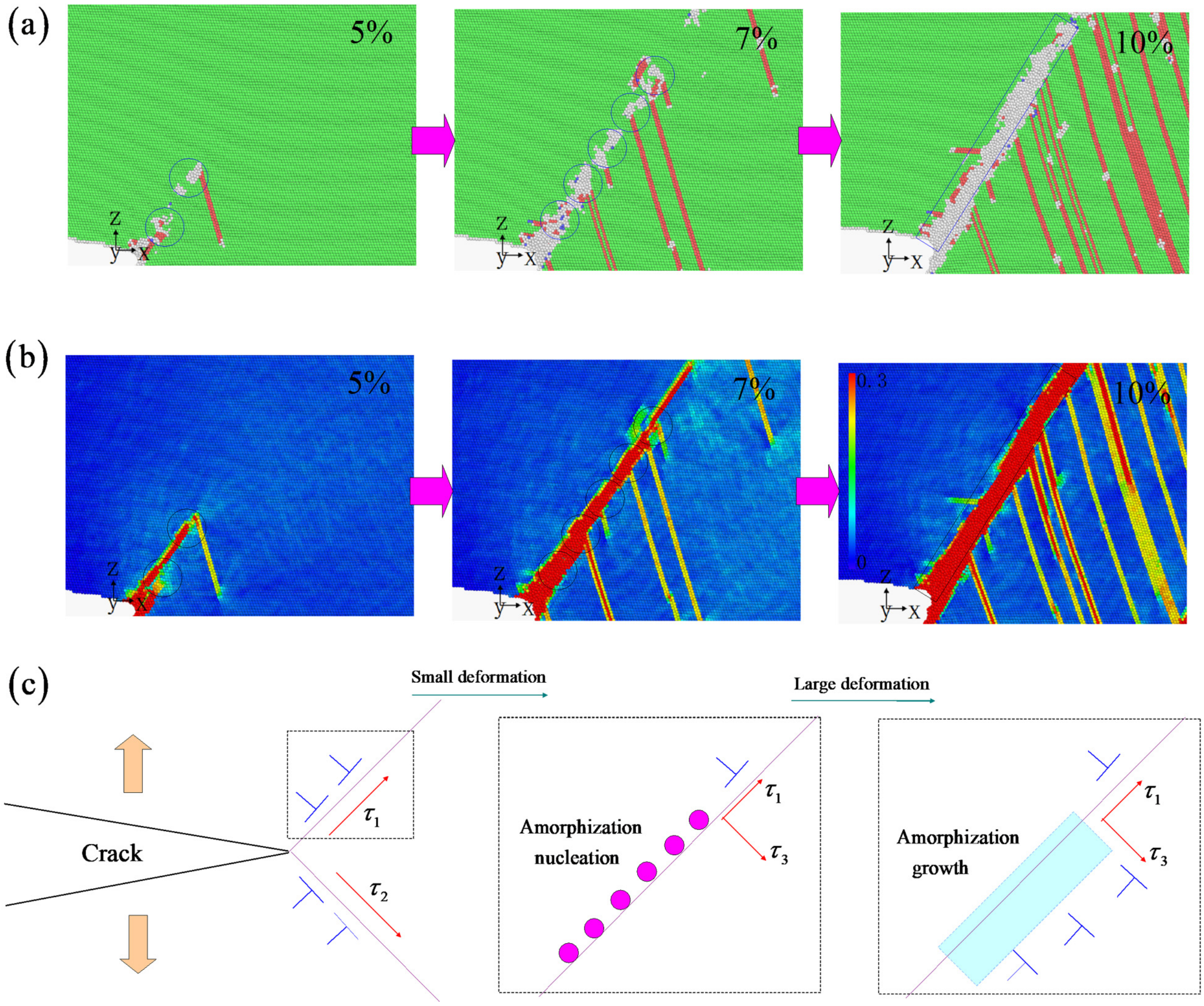

FIG. 10. The evolution of microstructure (a) and strain (b) from MD simulations. The schematic diagram for the occurrence of amorphization under a mode-I loading condition (c). (a)–(c) Amorphization nucleation, and amorphous growth. (c) The resolved shear stress, τ_3, induced by the serious lattice distortion and tension strain, drives the occurrence of dislocations and the structure transformation from crystallization to amorphization at the crack tip.

$E_{\rm dis} = \frac{\mu b^2 \rho}{10} + \frac{\mu b^2 \rho}{4\pi} \ln \frac{\rho^{-0.5}}{5b}$, in which μ is shear modulus which is about 80 GPa [72], $b = 0.255$ nm is the magnitude of Burger's vector [74], ρ is the dislocation density. The elastic part of the strain energy $E_{\rm ela}$ can be expressed as $E_{\rm ela} = \sigma_y^2/(2E)$. Therefore, the only variable in Eq. (6) is the dislocation density. Therefore, the variation of $r_{\rm crit}$ with dislocation density can be obtained as shown in Fig. 12. From Fig. 12, the values of $r_{\rm crit}$ decrease continuously with the

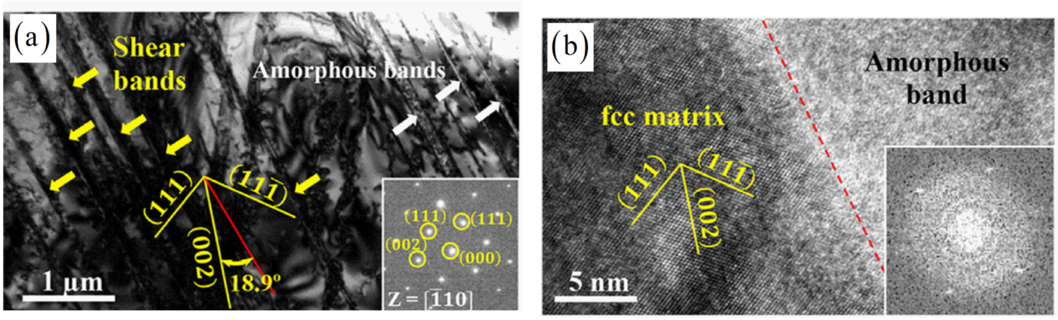

FIG. 11. (a) The TEM bright-filed micrographs with the corresponding selected area diffraction patterns inset, and (b) the corresponding high-resolution TEM image of the amorphous band, with the fast Fourier transform pattern inset confirming the presence of amorphous structure [68].

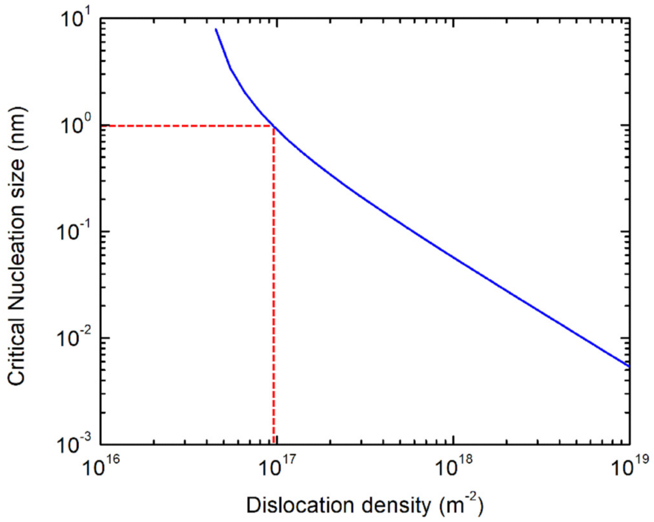

FIG. 12. The variation of critical size for a stable amorphous nucleus with dislocation density. The critical nucleation size of the present alloy was estimated on the order of 1 nm. The red dashed line indicates that the corresponding critical dislocation density in which the amorphization would take place is about $9.54 \times 10^{16} \mathrm{m}^{-2}$.

increasing of dislocation density. The smaller r_{crit}, the more likely for the deformation-induced amorphization process to occur. The crystalline to amorphous transition usually occurs at the atomic-scale level. The amorphous region usually initiates from the dislocation core regions [75]. Therefore, the critical nucleation size of amorphous structure can be roughly estimated as the dislocation core width which is usually on the magnitude of several Burgers vectors [76]. Here, we take the critical nucleation size r_{crit} as about 1 nm for an estimation. Hence, the critical dislocation density ρ^* for the crystalline to amorphization transition can be estimated as about $9.54 \times 10^{16}\ \mathrm{m}^{-2}$. In Table I, the critical dislocation density agrees with the result of MD simulations (see Fig. 13 and Figs. S4 and S5 [37]), indicating the nucleation of amorphization to easily occur in $(\bar{1}10)\langle 110\rangle$. The dislocation density can be computed by $\rho = n/S$, where n is the number of dislocation, and S is the area of crack tip. Furthermore, the crystalline to amorphous transitions occur in HEAs after radiation [77], due to the significant change of various lattice distortion and instability at high atomic-level stresses through irradiation. Therefore, in the crack plane $(\bar{1}10)\langle 110\rangle$, the higher flow stress and dislocation density result in the structure transition from crystalline to amorphous phase. Recent experiment also confirms the formation of amorphous phase due to the high density of dislocation [68].

TABLE I. Interface energy between crystal and amorphous phase, free-energy change from crystal to amorphous phase, and dislocation density.

Crystallographic orientation	[100]	[110]	[111]
Interface energy ($\mathrm{mJ/m^2}$)	369.5	506.3	575.8
Free energy (kJ/mol)	3.68	4.73	4.63
Dislocation density ($10^{16}\mathrm{m}^{-2}$)	7.5 ± 0.5	17.5 ± 0.6	2.8 ± 0.6

V. CONCLUSION

To investigate the unstable cracking behavior on a nanoscale, we used an atomistic-simulation technique to investigate the effect of crystal orientations on crack-propagation behaviors in the single-crystal HEA. The crystal orientations can strongly affect the deformation mechanisms at crack tip: (1) for the $(001)\langle 110\rangle$ orientation, the deformation twinning and dislocation activation along multislip systems take place; (2) for the $(\bar{1}10)\langle 110\rangle$ orientation, the amorphous nucleation occurs; and (3) for the $(1\bar{1}\bar{1})\langle 110\rangle$ orientation, the wavy slip is formed. Thus, the formation of deformation twinning, the occurrence of amorphization, and the emission of dislocations activated in multislip systems are observed and rely on the crystal orientation during crack propagation. Especially, the previous experiments show the amorphization at the crack tip is hard to happen. This process contributes to enhancing the damage tolerance in ductile HEAs. It also demonstrates that the severe atomic-scale lattice distortion is atomic-scale origins of high damage tolerance at cryogenic temperatures in HEAs. This approach can be further utilized to design the advanced HEAs with the high damage tolerance via controlling the crack propagation along the special crystallographic path by means of changing elemental concentration, elemental composition, and crystal growth

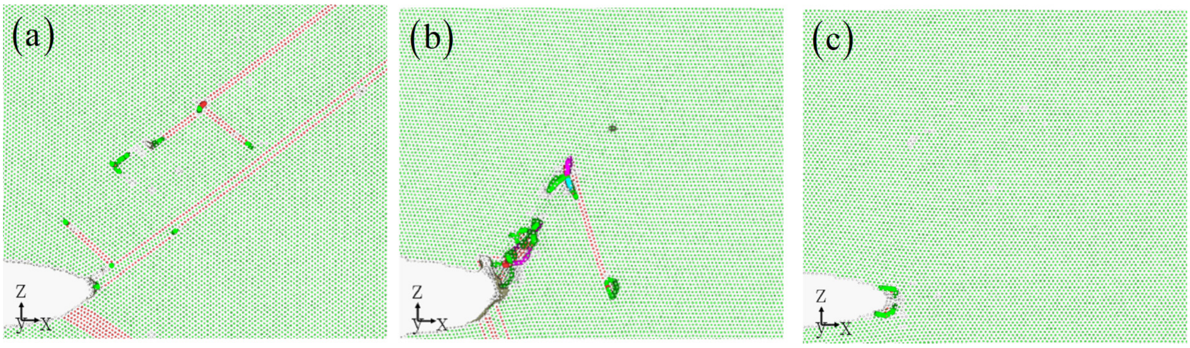

FIG. 13. Dislocation structure of crack tip at strain of 12% and the different crack-plane orientations: $(001)\langle 110\rangle$, $(\bar{1}10)\langle 110\rangle$, and $(1\bar{1}\bar{1})\langle 110\rangle$. Dislocations are displayed according to the dislocation extraction algorithm (DXA): Perfect dislocations of deep blue, Shockley dislocations of green, Stair-rod dislocations of pink, Hirth dislocations of yellow, Frank dislocations of light blue, and unidentified dislocations of red.

direction. In the future, the multitarget magnetron sputtering technology combined with the heat treatment would provide an effective regulation on important issues.

ACKNOWLEDGMENTS

The authors deeply appreciate the support from the Foundation for Innovative Research Groups of the National Natural Science Foundation of China (Grant No. 51621004), and the National Natural Science Foundation of China (Grants No. 11772122, No. 51871092, and No. 51771232). The research of Y.Y. is supported by City University of Hong Kong with Grant No. 9610391 and by Research Grants Council (RGC), the Hong Kong government through the General Research Fund (GRF) with Grant No. 11207215. P.K.L. very much appreciates the support of the U.S. Army Research Office Project (Grants No. W911NF-13-1-0438 and No. W911NF-19-2-0049) with the program managers, Dr. M. P. Bakas, Dr. S. N. Mathaudhu, and Dr. D. M. Stepp. P.K.L. acknowledges the support from the National Science Foundation (Grants No. DMR-1611180 and No. 1809640) with the program directors, Dr. J. Yang, Dr. J. G. Shiflet, and Dr. D. Farkas.

The authors declare no competing interest.

[1] B. Gludovatz, A. Hohenwarter, D. Catoor, E. H. Chang, E. P. George, and R. O. Ritchie, A fracture-resistant high-entropy alloy for cryogenic applications, Science **345**, 1153 (2014).

[2] Z. Li, K. G. Pradeep, Y. Deng, D. Raabe, and C. C. Tasan, Metastable high-entropy dual-phase alloys overcome the strength-ductility trade-off, Nature (London) **534**, 227 (2016).

[3] Y. Zhang, T. T. Zuo, Z. Tang, M. C. Gao, K. A. Dahmen, P. K. Liaw, and Z. P. Lu, Microstructures and properties of high-entropy alloys, Prog. Mater. Sci. **61**, 1 (2014).

[4] Z. Zhang, M. M. Mao, J. Wang, B. Gludovatz, Z. Zhang, S. X. Mao, E. P. George, Q. Yu, and R. O. Ritchie, Nanoscale origins of the damage tolerance of the high-entropy alloy CrMnFeCoNi, Nat. Commun. **6**, 10143 (2015).

[5] Z. Lei, X. Liu, Y. Wu, H. Wang, S. Jiang, S. Wang, X. Hui, Y. Wu, B. Gault, P. Kontis, D. Raabe, L. Gu, Q. Zhang, H. Chen, H. Wang, J. Liu, K. An, Q. Zeng, T. Nieh, and Z. Lu, Enhanced strength and ductility in a high-entropy alloy via ordered oxygen complexes, Nature (London) **563**, 546 (2018).

[6] T. Yang, Y. L. Zhao, Y. Tong, Z. B. Jiao, J. Wei, J. X. Cai, K. Lu, Y. Liu, and C. T. Liu, Multicomponent intermetallic nanoparticles and superb mechanical behaviors of complex alloys, Science **362**, 933 (2018).

[7] Q. Ding, Y. Zhang, X. Chen, X. Fu, D. Chen, S. Chen, L. Gu, F. Wei, H. Bei, Y. Gao, M. Wen, J. Li, Z. Zhang, T. Zhu, R. O. Ritchie, and Q. Yu, Tuning element distribution, structure and properties by composition in high-entropy alloys, Nature (London) **574**, 223 (2019).

[8] H. Oh, S. Kim, K. Odbadrakh, W. Ryu, K. Yoon, S. Mu, F. Körmann, Y. Ikeda, C. Tasan, D. Raabe, T. Egami, and E. Park, Engineering atomic-level complexity in high-entropy and complex concentrated alloys, Nat. Commun. **10**, 2090 (2019).

[9] Z. Tang, T. Yuan, C. W. Tsai, J. W. Yeh, C. D. Lundin, and P. K. Liaw, Fatigue behavior of a wrought $Al_{0.5}CoCrCuFeNi$ two-phase high-entropy alloy, Acta Mater. **99**, 247 (2015).

[10] M. A. Melia, S. R. Whetten, R. Puckett, M. Jones, M. J. Heiden, N. Argibay, and A. B. Kustas, High-throughput additive manufacturing and characterization of refractory high entropy alloys, Appl. Mater. Today **19**, 100560 (2020).

[11] Y. Bu, Z. Li, J. Liu, H. Wang, D. Raabe, and W. Yang, Nonbasal Slip Systems Enable a Strong and Ductile Hexagonal-Close-Packed High-Entropy Phase, Phys. Rev. Lett. **122**, 075502 (2019).

[12] C. Kenel, N. P. Casati, and D. C. Dunand, 3D ink-extrusion additive manufacturing of CoCrFeNi high-entropy alloy micro-lattices, Nat. Commun. **10**, 904 (2019).

[13] P. Shi, W. Ren, T. Zheng, Z. Ren, X. Hou, J. Peng, and P. K. Liaw, Enhanced strength–ductility synergy in ultrafine-grained eutectic high-entropy alloys by inheriting microstructural lamellae, Nat. Commun. **10**, 489 (2019).

[14] F. Granberg, K. Nordlund, M. W. Ullah, K. Jin, C. Lu, H. Bei, and Y. Zhang, Mechanism of Radiation Damage Reduction in Equiatomic Multicomponent Single Phase Alloys, Phys. Rev. Lett. **116**, 135504 (2016).

[15] M. Song, R. Zhou, J. Gu, Z. Wang, S. Ni, and Y. Liu, Nitrogen induced heterogeneous structures overcome strength-ductility trade-off in an additively manufactured high-entropy alloy, Appl. Mater. Today **18**, 100498 (2020).

[16] K. Ming, X. Bi, and J. Wang, Realizing strength-ductility combination of coarse-grained $Al_{0.2}Co_{1.5}CrFeNi_{1.5}Ti_{0.3}$ alloy via nano-sized, coherent precipitates, Int. J. Plast. **100**, 177 (2018).

[17] J. Li, H. Chen, Q. Fang, C. Jiang, Y. Liu, and P. K. Liaw, Unraveling the dislocation–precipitate interactions in high-entropy alloys, Int. J. Plast. **133**, 102819 (2020).

[18] I. A. Ovid'ko, R. Z. Valiev, and Y. T. Zhu, Review on superior strength and enhanced ductility of metallic nanomaterials, Prog. Mater. Sci. **94**, 462 (2018).

[19] O. El-Atwani, N. Li, M. Li, A. Devaraj, J. K. S. Baldwin, M. M. Schneider, and E. Martinez, Outstanding radiation resistance of tungsten-based high-entropy alloys, Sci. Adv. **5**, eaav2002 (2019).

[20] Q. Fang, Y. Chen, J. Li, C. Jiang, B. Liu, Y. Liu, and P. K. Liaw, Probing the phase transformation and dislocation evolution in dual-phase high-entropy alloys, Int. J. Plast. **114**, 161 (2018).

[21] S. Liu, M. C. Gao, P. K. Liaw, and Y. Zhang, Microstructures and mechanical properties of $Al_xCrFeNiTi_{0.25}$ alloys, J. Alloys Compd. **619**, 610 (2015).

[22] Y. Zou, H. Ma, and R. Spolenak, Nanocrystalline high-entropy alloys: A new paradigm in high-temperature strength and stability, Nat. Commun. **6**, 7748 (2015).

[23] M. Bahramyan, R. T. Mousavian, and D. Brabazon, Determination of atomic-scale structure and compressive behavior of solidified AlxCrCoFeCuNi high entropy alloys, Int. J. Mech. Sci. **171**, 105389 (2020).

[24] M. Bahramyan, R. T. Mousavian, and D. Brabazon, Study of the plastic deformation mechanism of TRIP-TWIP high entropy alloys at the atomic level, Int. J. Plast. **127**, 102649 (2020).

[25] Y. Afkham, M. Bahramyan, R. T. Mousavian, and D. Brabazon, Tensile properties of AlCrCoFeCuNi glassy alloys: A molecular dynamics simulation study, Mater. Sci. Eng. A **698**, 143 (2017).

[26] A. Sharma, P. Singh, D. D. Johnson, P. K. Liaw, and G. Balasubramanian, Atomistic clustering-ordering and high-strain deformation of an $Al_{0.1}$CrCoFeNi high-entropy alloy, Sci. Rep. **6**, 31028 (2016).

[27] A. Sharma and G. Balasubramanian, Dislocation dynamics in Al0.1CoCrFeNi high-entropy alloy under tensile loading, Intermetallics **91**, 31 (2017).

[28] A. Sharma, S. A. Deshmukh, P. K. Liaw, and G. Balasubramanian, Crystallization kinetics in Al_xCrCoFeNi ($0 \leqslant x \leqslant 40$) high-entropy alloys, Scr. Mater. **141**, 54 (2017).

[29] A. Sharma, R. Singh, P. K. Liaw, and G. Balasubramanian, Cuckoo searching optimal composition of multicomponent alloys by molecular simulations, Scr. Mater. **130**, 292 (2017).

[30] Z. H. Aitken, V. Sorkin, and Y. W. Zhang, Atomistic modeling of nanoscale plasticity in high-entropy alloys, J. Mater. Res. **34**, 1509 (2019).

[31] J. Li, Q. Fang, B. Liu, and Y. Liu, Transformation induced softening and plasticity in high entropy alloys, Acta Mater. **147**, 35 (2018).

[32] Z. H. Aitken and Y. W. Zhang, Revealing the deformation twinning nucleation mechanism of BCC HEAs, MRS Commun. **9**, 406 (2019).

[33] E. Ghassemali, R. Sonkusare, K. Biswas, and N. P. Gurao, In-situ study of crack initiation and propagation in a dual phase AlCoCrFeNi high entropy alloy, J. Alloys Compd. **710**, 539 (2017).

[34] H. Jia, G. Wang, S. Chen, Y. Gao, W. Li, and P. K. Liaw, Fatigue and fracture behavior of bulk metallic glasses and their composites, Prog. Mater. Sci. **98**, 168 (2018).

[35] W. Fang, H. X. Xie, F. X. Yin, J. Li, D. F. Khan, and Q. Fang, Molecular dynamics simulation of grain boundary geometry on crack propagation of bi-crystal aluminum, Mater. Sci. Eng. A **666**, 314 (2016).

[36] L. Pei, C. Lu, X. Zhao, L. Zhang, K. Cheng, G. Michal, and K. Tieu, Brittle versus ductile behaviour of nanotwinned copper: a molecular dynamics study, Acta Mater. **89**, 1 (2015).

[37] See Supplemental Material at http://link.aps.org/supplemental/10.1103/PhysRevMaterials.4.103612 for crack propagation, element distribution, and dislocation behavior.

[38] W. M. Choi, Y. H. Jo, S. S. Sohn, S. Lee, and B. J. Lee, Understanding the physical metallurgy of the CoCrFeMnNi high-entropy alloy: An atomistic simulation study, NPJ Comput. Mater. **4**, 1 (2018).

[39] B. J. Lee, M. I. Baskes, H. Kim, and Y. K. Cho, Second nearest neighbor modified embedded atom method potentials for BCC transition metals, Phys. Rev. B **64**, 184102 (2001).

[40] B. J. Lee, J. H. Shim, and H. M. Park, A semiempirical atomic potential for the FeCr binary system, Calphad **25**, 527 (2001).

[41] B. J. Lee, J. H. Shim, and M. I. Baskes, Semiempirical atomic potentials for the FCC metals Cu, Ag, Au, Ni, Pd, Pt, Al, and Pb based on first and second nearest neighbor modified embedded atom method, Phys. Rev. B **68**, 144112 (2003).

[42] W. M. Choi, Y. M. Kim, D. H. Seol, and B. J. Lee, Modified embedded atom method interatomic potentials for the CoCr, CoFe, CoMn, CrMn, and MnNi binary systems, Comput. Mater. Sci. **130**, 121 (2007).

[43] W. P. Dong, H. K. Kim, W. S. Ko, B. M. Lee, and B. J. Lee, Atomistic modeling of pure Co and CoAl system, Calphad **38**, 7 (2012).

[44] Y. M. Kim, Y. H. Shin, and B. J. Lee, Modified embedded atom method interatomic potentials for pure Mn and FeMn system, Acta Mater. **57**, 474 (2009).

[45] Y. K. Kim, W. S. Jung, and B. J. Lee, Modified embedded atom method interatomic potentials for the NiCo binary and the NiAlCo ternary systems, Model. Simul. Mater. Sci. Eng. **23**, 055004 (2015).

[46] C. Wu, B. J. Lee, and X. Su, Modified embedded atom interatomic potential for FeNi, CrNi, and FeCrNi systems, Calphad **57**, 98 (2017).

[47] S. Plimpton, Fast parallel algorithms for short-range molecular dynamics, J. Comput. Phys. **117**, 1 (1995).

[48] A. Stukowski, Visualization and analysis of atomistic simulation data with OVITO–the open visualization tool, Model. Simul. Mater. Sci. Eng. **18**, 015012 (2009).

[49] B. Lawn, *Fracture of Brittle Solids* (Cambridge Solid State Science Series, Cambridge, 1993).

[50] A. A. Griffith and M. Eng, The phenomena of rupture and flow in solids, Philos. Trans. R. Soc. London A **221**, 163 (1921).

[51] E. B. Tadmor and S. Hai, A Peierls criterion for the onset of deformation twinning at a crack tip, J. Mech. Phys. Solids. **51**, 765 (2003).

[52] V. Yamakov, E. Saether, D. R. Phillips, and E. H. Glaessgen, Molecular-dynamics simulation-based cohesive zone representation of intergranular fracture processes in aluminum, J. Mech. Phys. Solids. **54**, 1899 (2006).

[53] J. R. Rice, Dislocation nucleation from a crack tip: An analysis based on the Peierls concept, J. Mech. Phys. Solids. **40**, 239 (1992).

[54] J. Chen, S. N. Mathaudhu, N. Thadhani, and A. M. Dongare, Correlations between dislocation density evolution and spall strengths of Cu/Ta multilayered systems at the atomic scales: The role of spacing of KS interfaces, Materialia. **5**, 100192 (2019).

[55] A. Shekhawat, S. Zapperi, and J. P. Sethna, From Damage Percolation to Crack Nucleation through Finite Size Criticality, Phys. Rev. Lett. **110**, 185505 (2013).

[56] L. R. Owen, E. J. Pickering, H. Y. Playford, H. J. Stone, M. G. Tucker, and N. G. Jones, An assessment of the lattice strain in the CrMnFeCoNi high-entropy alloy, Acta Mater. **122**, 11 (2017).

[57] P. Singh, A. V. Smirnov, and D. D. Johnson, Atomic short-range order and incipient long-range order in high-entropy alloys, Phys. Rev. B **91**, 224204 (2015).

[58] Z. Wu and W. A. Curtin, Brittle and ductile crack-tip behavior in magnesium, Acta Mater. **88**, 1 (2015).

[59] C. Jiang and S. G. Srinivasan, Unexpected strain-stiffening in crystalline solids, Nature (London) **496**, 339 (2013).

[60] Y. Wu, F. Zhang, X. Yuan, H. Huang, X. Wen, Y. Wang, M. Zhang, H. Wu, X. Liu, H. Wang, S. Jiang, and Z. Lu, Short-range ordering and its effects on mechanical properties of high-entropy alloys, J. Mater. Sci. Technol. **62**, 214 (2021).

[61] R. Zhang, S. Zhao, J. Ding, Y. Chong, T. Jia, C. Ophus, M. Asta, R. O. Ritchie, and A. M. Minor, Short-range order and its impact on the CrCoNi medium-entropy alloy, Nature (London) **581**, 283 (2020).

[62] B. Yin, S. Yoshida, N. Tsuji, and W. A. Curtin, Yield strength and misfit volumes of NiCoCr and implications for short-range-order, Nat. Commun. **11**, 2507 (2020).

[63] J. Ding, Q. Yu, M. Asta, and R. O. Ritchie, Tunable stacking fault energies by tailoring local chemical order in CrCoNi medium-entropy alloys, Proc. Natl. Acad. Sci. USA **115**, 8919 (2018).

[64] S. Huang, H. Huang, W. Li, D. Kim, S. Lu, X. Li, and L. Vitos, Twinning in metastable high-entropy alloys, Nat. Commun. **9**, 2381 (2018).

[65] Y. C. Yang, C. Liu, C. Y. Lin, and Z. Xia, Core effect of local atomic configuration and design principles in Al_xCoCrFeNi high-entropy alloys, Scr. Mater. **178**, 181 (2020).

[66] P. R. Okamoto, J. K. Heuer, N. Q. Lam, S. Ohnuki, Y. Matsukawa, K. Tozawa, and J. F. Stubbins, Stress-induced amorphization at moving crack tips in NiTi, Appl. Phys. Lett. **73**, 473 (1998).

[67] E. Ma, Amorphization in mechanically driven material systems, Scr. Mater. **49**, 941 (2003).

[68] K. S Ming, W. J. Lu, Z. M. Li, X. F. Bi, and J. Wang, Amorphous bands induced by low temperature tension in a non-equiatomic CrMnFeCoNi alloy, Acta Mater. **188**, 354 (2020).

[69] W. Wu, S. Ni, Y. Liu, B. Liu, and M. Song, Amorphization at twin-twin intersected region in FeCoCrNi high-entropy alloy subjected to high-pressure torsion, Mater. Charact. **127**, 111 (2017).

[70] E. R. Leite and C. Ribeiro, *Crystallization and Growth of Colloidal Nanocrystals* (Springer, New York, 2012).

[71] J. W. Christian, *The Theory of Transformations in Metals and Alloys* (Pergamon, Oxford, 2002).

[72] Z. Wu, H. Bei, G. M. Pharr, and E. P. George, Temperature dependence of the mechanical properties of equiatomic solid solution alloys with face-centered cubic crystal structures, Acta Mater. **81**, 428 (2014).

[73] K. K. Chawla and M. A. Meyers, *Mechanical Behavior of Materials* (Cambridge University Press, Cambridge, 2008).

[74] C. Zhu, Z. P. Lu, and T. G. Nieh, Incipient plasticity and dislocation nucleation of FeCoCrNiMn high-entropy alloy, Acta Mater. **61**, 2993 (2013).

[75] J. Y. Huang, Y. T. Zhu, X. Z. Liao, and R. Z. Valiev, Amorphization of TiNi induced by high-pressure torsion, Philos. Mag. Lett. **84**, 183 (2004).

[76] A. Hunter, R. F. Zhang, and I. J. Beyerlein, The core structure of dislocations and their relationship to the material γ-surface, J. Appl. Phys. **115**, 134314 (2014).

[77] T. Egami, W. Guo, P. D. Rack, and T. Nagase, Irradiation resistance of multicomponent alloys, Metall. Mater. Trans. A **45**, 180 (2013).